ARTICLES
https://doi.org/10.1038/s41563-022-01245-x

nature materials

Check for updates

Coupling between magnetic order and charge transport in a two-dimensional magnetic semiconductor

Evan J. Telford[1,2], Avalon H. Dismukes[1], Raymond L. Dudley[2], Ren A. Wiscons[1], Kihong Lee[1], Daniel G. Chica[1], Michael E. Ziebel[1], Myung-Geun Han[3], Jessica Yu[1], Sara Shabani[2], Allen Scheie[4], Kenji Watanabe[5], Takashi Taniguchi[6], Di Xiao[7,8], Yimei Zhu[3], Abhay N. Pasupathy[2,3], Colin Nuckolls[1], Xiaoyang Zhu[1], Cory R. Dean[2] ✉ and Xavier Roy[1] ✉

Semiconductors, featuring tunable electrical transport, and magnets, featuring tunable spin configurations, form the basis of many information technologies. A long-standing challenge has been to realize materials that integrate and connect these two distinct properties. Two-dimensional (2D) materials offer a platform to realize this concept, but known 2D magnetic semiconductors are electrically insulating in their magnetic phase. Here we demonstrate tunable electron transport within the magnetic phase of the 2D semiconductor CrSBr and reveal strong coupling between its magnetic order and charge transport. This provides an opportunity to characterize the layer-dependent magnetic order of CrSBr down to the monolayer via magnetotransport. Exploiting the sensitivity of magnetoresistance to magnetic order, we uncover a second regime characterized by coupling between charge carriers and magnetic defects. The magnetoresistance within this regime can be dynamically and reversibly tuned by varying the carrier concentration using an electrostatic gate, providing a mechanism for controlling charge transport in 2D magnets.

Layered A-type antiferromagnets are composed of van der Waals sheets with intralayer ferromagnetic (FM) order and interlayer antiferromagnetic (AFM) coupling[1]. Upon the application of an external magnetic field, the interlayer AFM order can be switched to a field-induced FM configuration, accompanied by a change in optical and electronic properties[2–6]. This change of spin structure produces emergent phenomena, including giant tunnelling magnetoresistance in vertical van der Waals spin filters[4,7,8], giant second harmonic generation in the AFM state due to the breaking of inversion symmetry by magnetic order[9] and magnetic-order-dependent excitonic transitions arising from changes in interlayer hybridization[2]. For applications in spin-based electronics, ideal materials should have functional semiconducting transport properties coupled with layered magnetism, which would allow for simultaneous control over charge and spin carriers. In studies of bulk magnetic semiconductors, magnetic defects and impurities play a crucial role in determining the magnetic and electronic properties. To further develop 2D magnetic semiconductors, it is thus critical to understand how magnetic order and magnetic defects couple to charge carriers[10–12,15]. In currently available 2D magnets, however, active modulation of charge transport properties via electrostatic gating remains a challenge, and the role of defects is essentially unexplored[13–15].

In this work, we report the magnetotransport properties of atomically thin CrSBr, a 2D van der Waals material with strongly coupled, layered A-type AFM order and semiconducting transport properties. Each CrSBr layer consists of two buckled rectangular planes of CrS fused together, with both surfaces capped by Br atoms (Fig. 1a)[3,16,17]. Stacking of the layers along the *c* axis produces an orthorhombic structure with space group *Pmmn*. The paramagnetic (PM)-to-AFM phase transition includes substantial intralayer FM correlations developing above the Néel temperature ($T_N = 132$ K) at a characteristic temperature ($T_c = 160$ K), as identified by heat capacity[9] and magnetic susceptibility[3] measurements. Below T_N, the layers order ferromagnetically, with spins oriented along the *b* axis, and align antiferromagnetically along the stacking direction (Fig. 1a)[3,16]. Crystals of CrSBr can be mechanically exfoliated, and a recent second harmonic generation study confirms that the bulk magnetic structure persists down to the FM monolayer and AFM bilayer[9].

In bulk single crystals, CrSBr is an extrinsic semiconductor with a direct bandgap of ~1.5 eV and finite conductivity that can be measured down to liquid helium temperature[3]. We find that the transport properties of few-layer CrSBr are dominated by the interlayer magnetic order. When the flakes are polarized with an external magnetic field, their resistances decrease drastically due to differences in interlayer spin-flip scattering between the AFM and FM configurations. In monolayer CrSBr, spin-flip scattering arises only from intraplanar FM ordering, which manifests as a peak of negative magnetoresistance near the monolayer Curie temperature

[1]Department of Chemistry, Columbia University, New York, NY, USA. [2]Department of Physics, Columbia University, New York, NY, USA. [3]Condensed Matter Physics and Materials Science Department, Brookhaven National Laboratory, Upton, NY, USA. [4]Neutron Scattering Division, Oak Ridge National Laboratory, Oak Ridge, TN, USA. [5]Research Center for Functional Materials, National Institute for Materials Science, Tsukuba, Japan. [6]International Center for Materials Nanoarchitectonics, National Institute for Materials Science, Tsukuba, Japan. [7]Department of Materials Science and Engineering, University of Washington, Seattle, WA, USA. [8]Department of Physics, University of Washington, Seattle, WA, USA. ✉e-mail: cd2478@columbia.edu; xr2114@columbia.edu

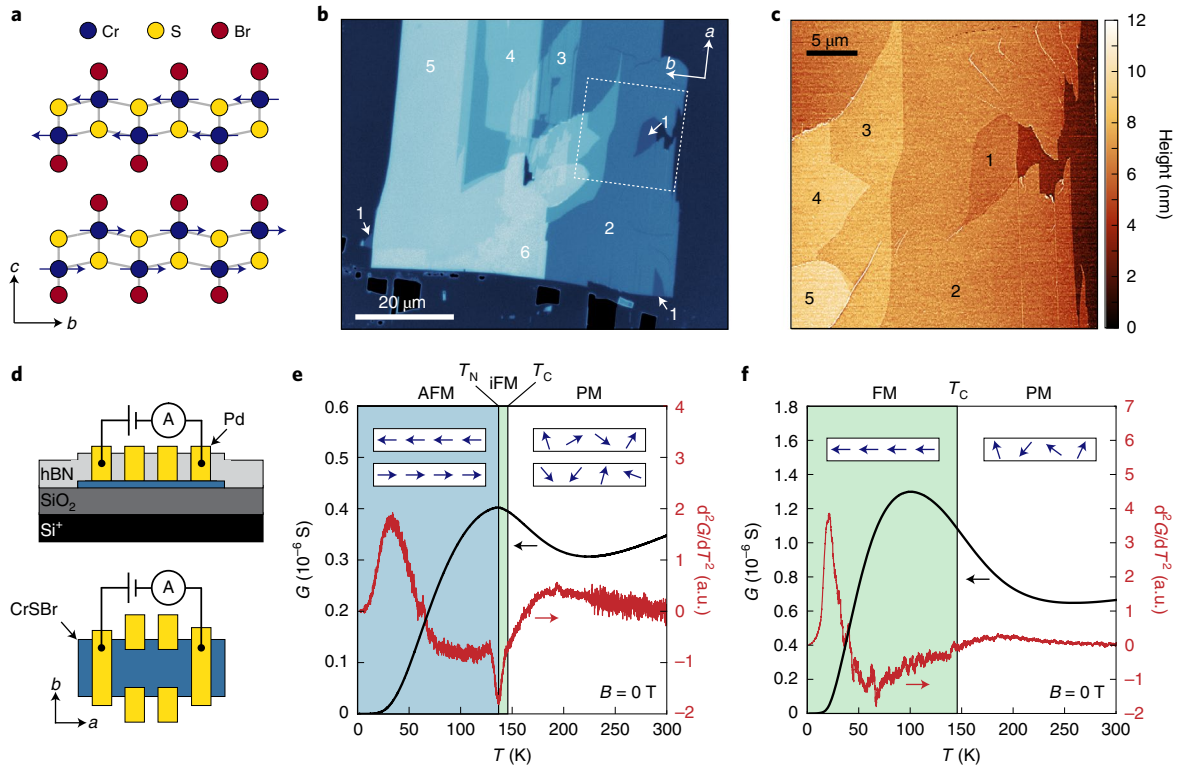

Fig. 1 | Crystal structure, device fabrication and transport signatures of CrSBr magnetic ordering. a, Crystal structure of CrSBr as viewed along the *a* axis. Orientations of the Cr spins in the AFM state are given by solid blue arrows. Blue, yellow and red circles correspond to Cr, S and Br, respectively. **b**, False-coloured optical image of an exfoliated CrSBr flake with thicknesses ranging from one to six layers. The corresponding layer numbers are denoted on the image. The orientation of the crystal axes is given in the upper right inset. **c**, Atomic force microscopy image of the CrSBr flake shown in **b**. The region where the image was taken is denoted by a dashed white box in **b**. The corresponding numbers of CrSBr layers are labelled on the image. **d**, Side-view (top) and top-view (bottom) schematics of the CrSBr device geometry. Colour code: hexagonal boron nitride (hBN), grey; Pd, yellow; SiO_2, dark grey; CrSBr, blue; Si^+ substrate, black. The orientation of the crystal axes relative to the electrodes is denoted. **e**,**f**, Conductance (solid black line) and second derivative of the conductance (solid red line) versus T at zero B for bilayer (**e**) and monolayer (**f**) CrSBr. The interlayer AFM, intralayer FM (labelled iFM or FM) and PM states are denoted by solid blue, solid green and white regions, respectively. T_N is defined as the location of the dip in d^2G/dT^2. T_C is defined from second harmonic generation measurements[9]. Cartoons of the spin orientation in each state are given in the insets. The white rectangles represent single CrSBr sheets, and the blue arrows represent the Cr spins.

($T_C = 146$ K (ref. [9])), followed by a drop to near zero upon cooling to ~40 K. For all layer numbers, magnetoresistance measurements reveal unexpected magnetic behaviour below 40 K, which we hypothesize originates from strong coupling between charge carriers and magnetic defects. In monolayer CrSBr we controllably switch between magnetoresistance mechanisms attributed to exchange interactions between free carriers and magnetic defects or magnetic polarons by varying the carrier density with an electrostatic gate.

Atomically thin CrSBr flakes are prepared via mechanical exfoliation on Si wafers with a 285-nm-thick SiO_2 layer (Supplementary Information for details)[18,19]. The thickness and crystallographic directions of exfoliated flakes are determined by optical contrast (Fig. 1b and Supplementary Figs. 1–3), atomic force microscopy (Fig. 1c and Supplementary Fig. 3) and Raman spectroscopy (Supplementary Figs. 4 and 5). Mesoscopic transport devices are fabricated using the via contact method[20], whereby palladium electrodes embedded in hexagonal boron nitride are transferred onto the desired CrSBr flakes using the dry-polymer-transfer process[21] (Fig. 1d; Supplementary Information for details). We performed electrical transport measurements as a function of temperature (T), magnetic field (B) and electrostatic gate voltage (V_{BG}) on CrSBr flakes ranging in thickness from one to nine layers. Current was sourced along the crystallographic *a* axis for all measurements (Fig. 1d). Owing to the high resistance of the flakes over the entire T range (Supplementary Figs. 6 and 7), all data reported in the main text were measured in a two-terminal configuration. Some measurements were repeated in a four-terminal configuration to confirm that the channel resistance dominates the transport properties (Supplementary Fig. 8).

Bilayer CrSBr displays an overall extrinsic semiconducting behaviour with conductance (G) decreasing with decreasing T (Fig. 1e). At $T = 136 \pm 4$ K, there is a sharp dip in the second derivative of G versus T (d^2G/dT^2), which is attributed to the onset of AFM ordering at T_N[3]. The G shows a local maximum at the same T due to reduced scattering caused by spin fluctuations as CrSBr becomes antiferromagnetically ordered[22,23]. Thicker flakes display similar features, signalling the onset of AFM order (Supplementary Fig. 9). Within experimental error, the values of T_N measured from transport for flakes ranging in thickness from two to nine layers are unchanged from the bulk value and independent of layer number (Supplementary Fig. 9). By contrast, monolayer CrSBr shows no dip in d^2G/dT^2 (Fig. 1f) but displays a zero crossing close to the expected monolayer T_C[9]. This is consistent with previous reports that monolayer CrSBr exhibits only intraplanar FM ordering[9]. Note that the low-T resistance for both bilayer and monolayer CrSBr is well described by Efros–Shklovskii variable range hopping, indicating that electronic transport is dominated by electron percolation

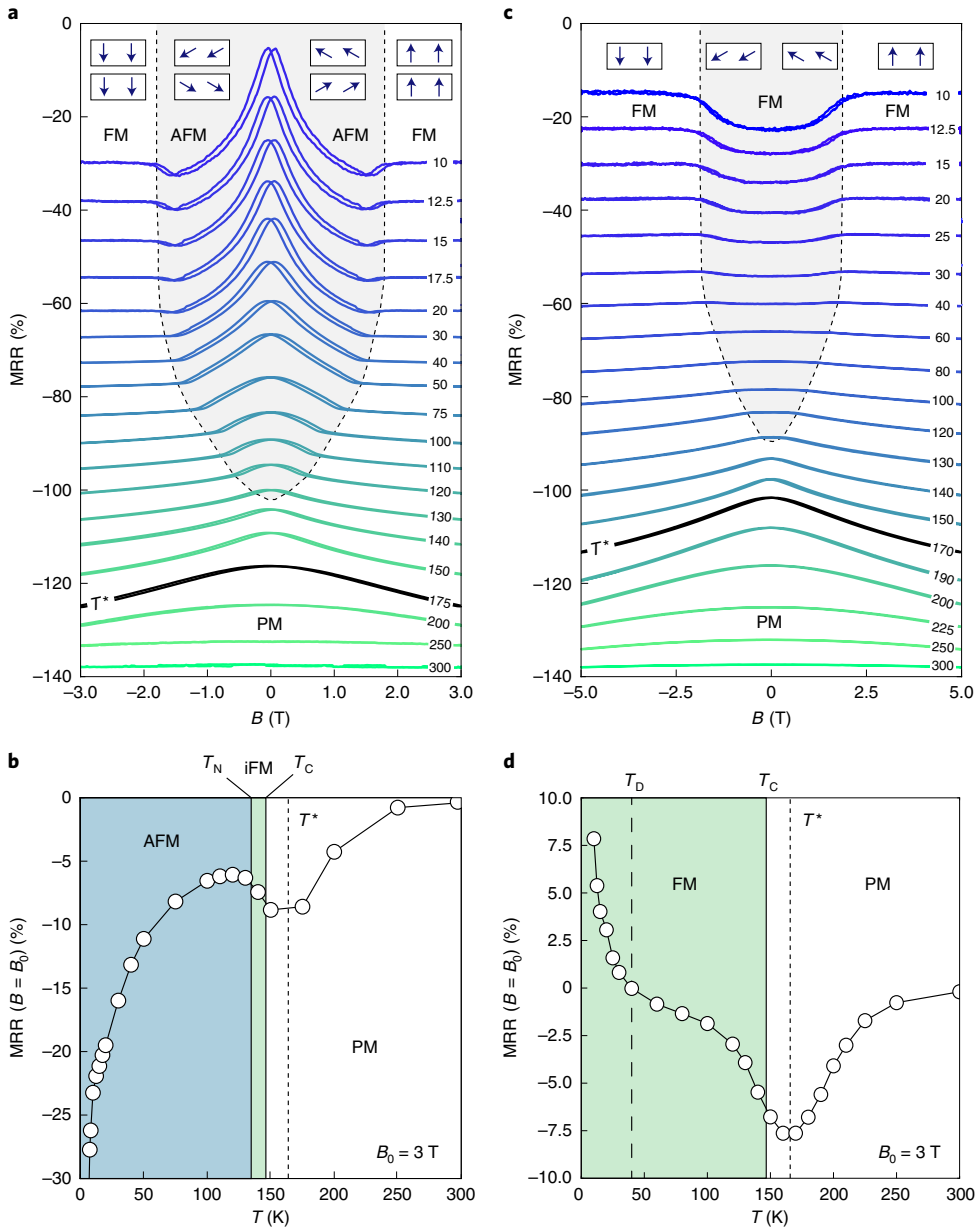

Fig. 2 | Magnetoresistance of bilayer and monolayer CrSBr. a,**c**, MRR versus B at various T with B oriented along the c axis for bilayer (**a**) and monolayer (**c**) CrSBr. Both forward and backward B sweeps are presented. The curves are offset for clarity. The solid black line is the curve taken near T^*, the temperature at which MRR has a local minimum. The corresponding magnetic phases are labelled, and B_{sat} is denoted by a dashed black line. Insets: schematics showing the orientation of the spins in each state. The white rectangles represent single CrSBr sheets, and the blue arrows represent the Cr spins. **b**,**d**, MRR at a fixed B parallel to the c axis versus T for bilayer (**b**) and monolayer (**d**) CrSBr. The B at which the fixed-field MRR is calculated is $B_0 = 3$ T. The interlayer AFM, intralayer FM (labelled iFM or FM) and PM phases are denoted by blue, green and white regions, respectively.

between hopping sites (Supplementary Fig. 10; Supplementary Fig. 11 for additional characterization)[24,25].

Figure 2a presents the magnetoresistance ratio (MRR) versus B and T for bilayer CrSBr. We define MRR $= \frac{R(B)-R(B=0)}{R(B=0)} \times 100$, where in this plot B is oriented along the c axis, and R is resistance. From 300 to ~175 K, the sample is in a PM phase characterized by a broad negative MRR (nMRR) due to the field-induced suppression of spin-flip scattering between conducting electrons and local magnetic moments[26,27]. The thermal fluctuations that prevent spins from aligning with B diminish with decreasing T, leading to an overall increase in the magnitude of the nMRR[15,23,28]. Below $T_N = 136 \pm 4$ K, we observe nMRR up to a well-defined saturation field (B_{sat}) beyond which the device resistance saturates with increasing B. This manifests as a dome of nMRR, the edges of which define B_{sat} (dashed black line in Fig. 2a). The magnitude of nMRR increases with decreasing T as the AFM state becomes more ordered, reaching −23.5% at 10 K (Fig. 2b; Supplementary Fig. 12 for lower T). This giant nMRR followed by saturation for $B > B_{sat}$ indicates that carrier scattering between layers is controlled by the interlayer magnetic configuration. In the AFM state at zero B, interlayer tunnelling is suppressed. As B increases, the spins are gradually canted towards the c axis, progressively breaking the AFM configuration and restoring interlayer tunnelling, which results in a decrease of the device resistance. At B_{sat}, the spins are fully polarized along the c axis, and a further increase of B has little effect on the resistance. Consistent with this understanding, all CrSBr samples thicker

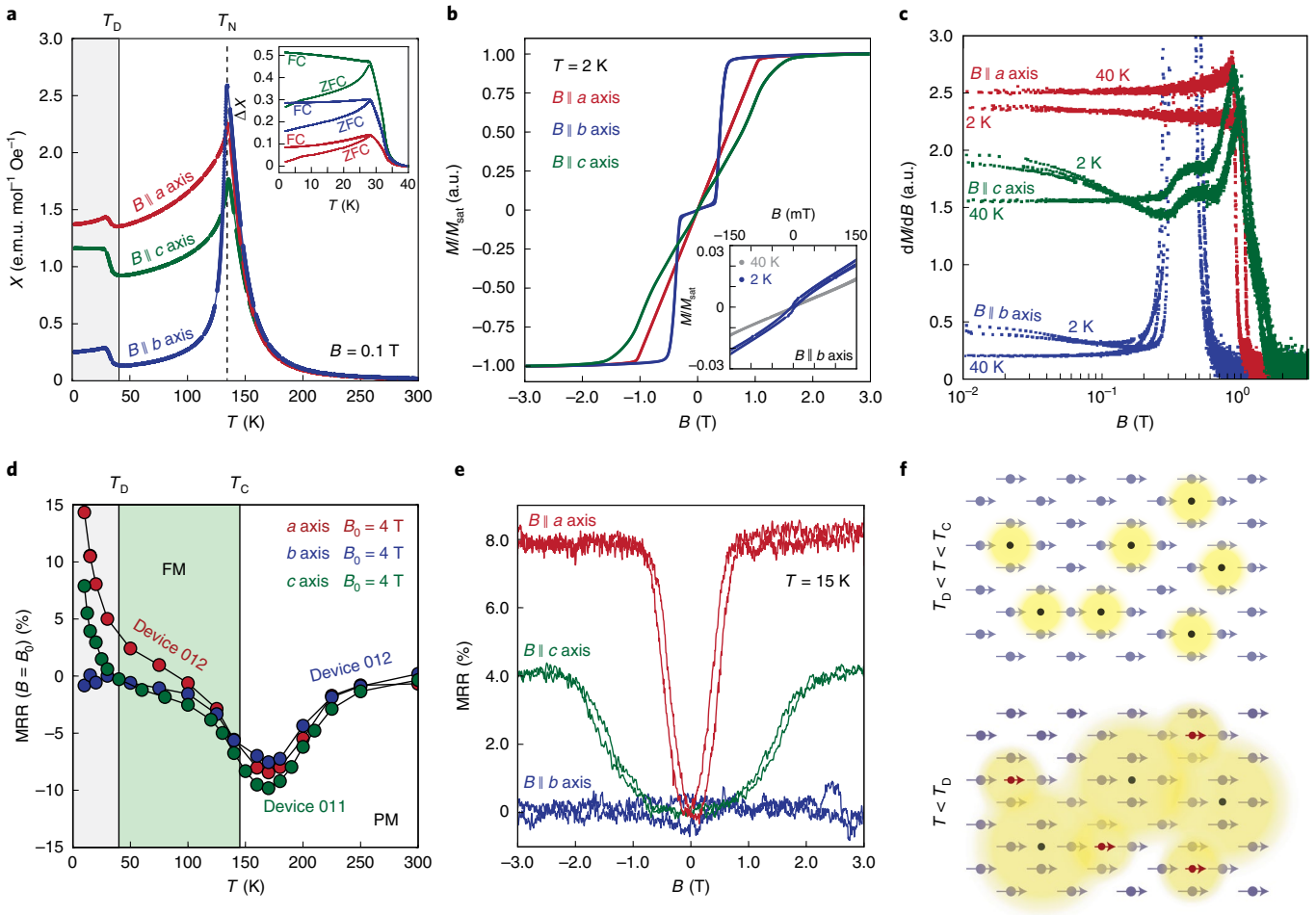

Fig. 3 | Evidence for coupling between charge transport and magnetic defects in CrSBr. a, Bulk χ versus T for $B = 0.1$ T oriented along the *a* axis (red), *b* axis (blue) and *c* axis (green). Top right inset: plot of the change in zero-field-cooled (ZFC) and field-cooled (FC) susceptibility across T_D with $B = 0.01$ T. **b**, Bulk M versus B at 2 K for B oriented along the *a* axis (red), *b* axis (blue) and *c* axis (green). The lower right inset plots the low-B M versus B for B along the *b* axis above (40 K, grey dots) and below (2 K, blue dots) T_D. All traces are normalized to the saturation magnetization (M_{sat}), defined as the M value when $B > B_{sat}$. **c**, The dM/dB versus B on a log scale above (40 K) and below (2 K) T_D for B oriented along the *a* axis (red), *b* axis (blue) and *c* axis (green). **d**, MRR at a fixed B versus T for B oriented along the *a* axis (red dots), *b* axis (blue dots) and *c* axis (green dots). The B at which the fixed-field MRR is calculated for each B direction (B_0) is given in the legend. The FM and PM phases are indicated by green and white regions, respectively. The labels Device 011 and Device 012 refer to measurements from two separate devices. **e,** MRR versus B in monolayer CrSBr for B oriented along the *a* axis (red), *b* axis (blue) and *c* axis (green). All curves were taken at 15 K, and both forward and backward B sweeps are presented. **f**, Schematic of the spin structure of monolayer CrSBr for $T_D < T < T_C$ (top) and $T < T_D$ (bottom). Cr spins, defect sites and polarized magnetic defect spins are denoted as blue arrows, black dots and red arrows, respectively. The yellow clouds represent the localization radius of the carriers.

than one layer exhibit the same qualitative MRR behaviour (Supplementary Figs. 13–16).

Figure 2c plots the magnetoresistance of the FM CrSBr monolayer versus B and T. Between 300 and 170 K, monolayer CrSBr exhibits the same behaviour as the multilayer samples in regards to nMRR, which we attribute to the suppression of spin-flip scattering in the PM state with increasing B, the magnitude of which increases as T decreases. As T is further lowered below 170 K, the magnitude of MRR decreases and approaches zero by 40 K (Fig. 2d). This is expected since the intralayer FM order reduces spin fluctuations at zero B, diminishing spin-flip scattering. The competition between these two phenomena leads to a peak in nMRR versus T at 170 K (black line in Fig. 2c), which we denote as T^*. This feature is present in all samples (black line in Fig. 2a for bilayer and bulk[3]), reflecting the onset of intraplanar FM correlations as it closely follows the monolayer T_C measured by second harmonic generation and the T_c determined from bulk heat capacity measurements[9]. T^* is the same for bilayer and monolayer CrSBr, indicating that this feature is independent of the interlayer AFM coupling. The remarkable agreement between transport and previous second harmonic generation results demonstrates that magnetotransport is a reliable probe of both FM and AFM order in CrSBr. Below 40 K (which we denote as T_D), monolayer CrSBr exhibits a positive MRR (pMRR) that increases with decreasing T (Fig. 2d). While this feature is most prominent in monolayer samples, it is also observed in the bilayer CrSBr sample in Fig. 2a (and in bulk CrSBr[3]) as a small pMRR just below B_{sat} (Supplementary Fig. 17 for a detailed analysis). Note that CrSBr devices fabricated from flakes greater than one layer thick exhibit hysteresis in MRR in the AFM state (Fig. 2a and Supplementary Figs. 13–16), which we attribute to the field-induced canted AFM state[29–31].

This low-T pMRR response is unexpected for a FM monolayer whose ordering temperature is well above 100 K. To better understand the origin of the pMRR, we performed magnetometry on bulk

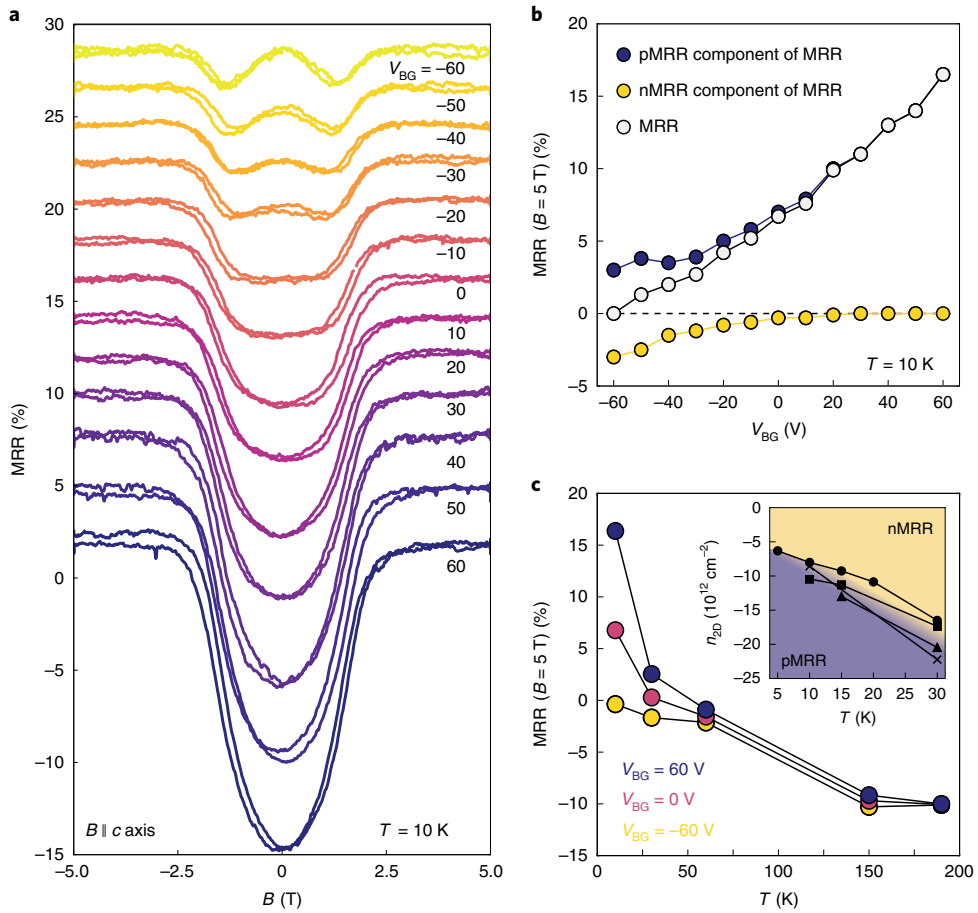

Fig. 4 | Electrostatic control of magnetoresistance in monolayer CrSBr. a, Monolayer CrSBr MRR versus B oriented along the c axis for various V_{BG} at 10 K. Both forward and backward B sweeps at each V_{BG} are presented. The curves are offset for clarity. The value of V_{BG} for each trace is denoted. **b**, MRR at 5 T (grey dots) and the corresponding extracted pMRR (blue dots) and nMRR (yellow dots) components versus V_{BG} at 10 K. **c**, MRR at 5 T versus T for V_{BG} = 60 V (blue dots), V_{BG} = 0 V (pink dots) and V_{BG} = −60 V (yellow dots). A phase diagram depicting the crossover between pMRR (blue region) and nMRR (yellow region) versus T and intrinsic sheet carrier density (n_{2D}) is given in the inset. Each data marker type corresponds to a different monolayer CrSBr device (four in total—black squares, black crosses, black circles and black triangles).

single crystals of CrSBr and complementary field-angle-dependent transport measurements on monolayer CrSBr (Fig. 3). The bulk magnetic susceptibility (χ) versus T curves (Fig. 3a) show the expected cusp at 134 ± 2 K associated with the AFM transition, followed by a sharp increase of χ beginning at ~35 K, which is unusual for an A-type antiferromagnet. The crystal structure of CrSBr is unchanged across this transition[3], and we observe an increase in χ for all B directions, which necessarily exempts structural transformation or spin reorientation as the origin of this feature. We also note that the increase in χ at low T resembles a FM transition. Consistent with this hypothesis, there is a divergence between the zero-field-cooled and field-cooled traces of χ versus T across the transition (inset of Fig. 3a). In Fig. 3b, we plot the magnetization (M) versus B at 2 K. The overall response is dominated by the AFM behaviour[3,16], characterized by a spin-flip transition at ~0.3 T along the easy b axis, and gradual canting of spins along the non-easy axes up to B_{sat}. However, if we focus on the low-B region along the easy axis, we observe the emergence of a small sigmoidal dependence below T_D, consistent with FM behaviour. The development of an additional FM phase is further evidenced by plotting dM/dB versus B (Fig. 3c) across the susceptibility transition. Above the transition (40 K), dM/dB is constant for all B directions up to ~0.2 T, but below the transition (2 K), there is an additional contribution to dM/dB at low B values[32]. A possible explanation for the emergence of FM features at low T is the existence of an impurity phase trapped in the bulk CrSBr crystals. However, such a phase would not be present in exfoliated flakes. Considering that monolayer and bulk CrSBr show similar low-T pMRR features[3], we believe the observed monolayer MRR anomalies at low T are related to the bulk susceptibility transition below T_D.

The MRR of monolayer CrSBr depends on the direction of B below T_D (Fig. 3e and Supplementary Fig. 18). The pMRR response is characterized by a quadratic dependence at low B followed by a saturation at B_{sat} when B is oriented along the intermediate axis (a axis) and the hard axis (c axis). When B is along the easy axis (b axis), there is negligible MRR, indicating that the spins are aligned along the b axis at zero B. The pMRR along the a and c axes therefore arises from a canting of the spins from the b axis towards the respective field directions, supported by the observation that the MRR saturation fields closely match the saturation fields in the bulk M-versus-B curves (Fig. 3b). The difference in magnitude of pMRR between the a and c axes is likely due to the anisotropic magnetoresistance effect, which produces pMRR when the magnetization direction is parallel to the source current direction[33]. For 40 K < T < 100 K, the data are consistent with the anisotropic magnetoresistance effect; MRR > 0 for fields parallel to the a axis, and MRR ≈ 0 for fields parallel to the c and b axes (Fig. 3d). Below 40 K, the MRR along the a and c axes increases drastically (Fig. 3d). The same anisotropy in MRR

was previously observed in bulk single-crystal transport measurements, in which pMRR features emerge along the *a* and *c* axes below ~40 K, but its origin was not explained[3].

Our magnetotransport data suggest strong coupling between charge transport and magnetic defects in the CrSBr lattice[34,35]. In analogous bulk magnetic semiconductor systems, magnetic defects can order collectively as a result of exchange interactions with localized charge carriers[36–38] or with the intrinsic magnetic lattice[39,40]. In CrSBr, the low-T magnetic structure likely consists of the dominant Cr magnetic lattice and a sublattice of defect spins. The magnetometry data indicate that upon cooling below T_N, Cr spins within each layer order ferromagnetically, but the defects remain unpolarized (Fig. 3f, top). Below T_D, the magnetic defects appear to polarize and adopt a FM configuration (Fig. 3f, bottom). From the field-angle-dependent MRR measurements in monolayer CrSBr, we suspect the defect spins are aligned with the *b* axis. The fact that T_D is much lower than T_N suggests that the defect moments (red arrows in Fig. 3f, bottom) arise from self-trapped electrons near donor sites (known as magnetic polarons[39,40]), rather than intrinsic magnetic impurities. This is supported by energy-dispersive X-ray spectroscopy and X-ray photoelectron spectroscopy on parent CrSBr crystals, which show no evidence of foreign magnetic atoms (Supplementary Figs. 19 and 20).

The coupling between magnetic defects and charge carriers and the corresponding MRR response is predicted to depend upon carrier density, which in our device can be dynamically and reversibly tuned using an electrostatic gate (Supplementary Fig. 21). Figure 4a presents the MRR of monolayer CrSBr versus B at different V_{BG} values. Starting from 0 V, as we increase V_{BG} (increase electron density), we observe an increase in the pMRR response, from 7.6% up to 16.4%. Conversely, decreasing V_{BG} (decreasing electron density) decreases the pMRR, and a noticeable region of nMRR emerges below −20 V at low B. At a gate voltage of −60 V, the MRR reaches −0.4% with regions of nMRR followed by pMRR equal in magnitude when $B < B_{sat}$. Figure 4b plots the MRR versus V_{BG} along with the extracted pMRR and nMRR contributions. There is a direct competition between the nMRR and pMRR regimes; increasing the electron density ($V_{BG} > 0$) yields larger pMRR, while decreasing the electron density ($V_{BG} < 0$) diminishes the pMRR contribution and induces nMRR. Together, these produce a MRR that depends linearly on V_{BG}. The T dependence of the MRR at different V_{BG} values (Fig. 4c and Supplementary Fig. 22) shows that the slope of MRR versus V_{BG} decreases quickly with increasing T and is negligible above T_D. A similar effect is observed in bilayer CrSBr, indicating the same defect-mediated MRR mechanisms are present in multilayer samples (Supplementary Fig. 23). The sensitivity to doping is further supported by the air sensitivity of monolayer CrSBr flakes. By exposing a monolayer device to air for a period of three weeks (Supplementary Fig. 24), we were able to change the doping level and the sign and magnitude of the MRR at low T and reproduce the behaviour of a second monolayer device with lower intrinsic carrier density (Supplementary Figs. 25–28). The carrier density at which the MRR crosses from pMRR to nMRR increases as T increases and is consistent between multiple samples (inset of Fig. 4c).

The sensitivity of the MRR to carrier density supports the hypothesis that the magnetotransport properties of CrSBr at low T are governed by the magnetic defects. The two competing magnetoresistance features (pMRR and nMRR) indicate that the unique shapes of the MRR curves result from a competition between multiple mechanisms that dominate within certain carrier density ranges. The nMRR component is characteristic of magnetic polarons[34,35,41–43] and is consistent with our observation that decreasing the carrier density enhances the nMRR[44]. Furthermore, the carrier density at which MRR crosses from pMRR to nMRR (inset of Fig. 4c) is close to the estimated magnetic defect density from bulk susceptibility measurements (Supplementary Information for calculations), implying that we observe nMRR when the free carrier density is less than the bulk magnetic defect density[36]. However, the formation of magnetic polarons is generally not associated with a large pMRR. In dilute magnetic semiconductors, pMRR often results from a B-dependent broadening of the defect density of states due to s–d exchange between magnetic impurities and separate electronic defect states[34,35,42,43,45,46]. Since the magnetic defects in CrSBr most likely arise from self-trapped charges instead of magnetic dopants, the observed pMRR ostensibly originates from exchange interactions between mobile carriers and magnetic defects. The coexistence of these two MRR mechanisms suggests that CrSBr contains both magnetic and non-magnetic defects. At low carrier densities, magnetic polarons dominate the MRR behaviour, but above some threshold carrier density, exchange interactions between free carriers and magnetic defects result in pMRR. The formation of magnetic polarons in tandem with carrier-mediated exchange interactions is consistent with the emergence of bulk FM properties and electron transport in the variable range hopping limit[34,35,41,45].

Magnetotransport is typically an indirect probe of magnetism, but in CrSBr, it reveals in striking detail a rich magnetic structure and its intricate and tunable coupling to charge carriers. For bilayer and thicker flakes, T_N is independent of layer number, and a large nMRR emerges as the interlayer AFM configuration is broken. In monolayer CrSBr, intraplanar FM order gives rise to a peak of nMRR close to T_C. This nMRR feature is also present in multilayer flakes, signalling the existence of intraplanar FM correlations above T_N. We uncovered a hidden regime below 40 K resulting from coupling between charge carriers and magnetic defects. In monolayer CrSBr, the magnetic defects dominate the low-T MRR, which can be linearly tuned using an electrostatic gate. These results highlight the utility of multilayer CrSBr as a 2D magnet with giant intrinsic nMRR. In the monolayer, the sensitivity of MRR to carrier density presents a unique opportunity not only for fabricating tunable spintronic devices, but also for understanding and utilizing defects to engineer tunable properties in van der Waals magnets.

Online content

Any methods, additional references, Nature Research reporting summaries, source data, extended data, supplementary information, acknowledgements, peer review information; details of author contributions and competing interests; and statements of data and code availability are available at https://doi.org/10.1038/s41563-022-01245-x.

Received: 23 June 2021; Accepted: 29 March 2022;
Published online: 5 May 2022

References

1. Gibertini, M., Koperski, M., Morpurgo, A. F. & Novoselov, K. S. Magnetic 2D materials and heterostructures. *Nat. Nanotechnol.* **14**, 408–419 (2019).
2. Wilson, N. P. et al. Interlayer electronic coupling on demand in a 2D magnetic semiconductor. *Nat. Mater.* https://doi.org/10.1038/s41563-021-01070-8 (2021).
3. Telford, E. J. et al. Layered antiferromagnetism induces large negative magnetoresistance in the van der Waals semiconductor CrSBr. *Adv. Mater.* **32**, 2003240 (2020).
4. Klein, D. R. et al. Probing magnetism in 2D van der Waals crystalline insulators via electron tunneling. *Science* **360**, 1218–1222 (2018).
5. Deng, Y. et al. Quantum anomalous Hall effect in intrinsic magnetic topological insulator $MnBi_2Te_4$. *Science* **367**, 895–900 (2020).
6. Huang, B. et al. Layer-dependent ferromagnetism in a van der Waals crystal down to the monolayer limit. *Nature* **546**, 270–273 (2017).
7. Song, T. et al. Giant tunneling magnetoresistance in spin-filter van der Waals heterostructures. *Science* **360**, 1214–1218 (2018).
8. Kim, H. H. et al. Tailored tunnel magnetoresistance response in three ultrathin chromium trihalides. *Nano Lett.* **19**, 5739–5745 (2019).
9. Lee, K. et al. Magnetic order and symmetry in the 2D semiconductor CrSBr. *Nano Lett.* **21**, 3511–3517 (2021).
10. Chua, R. et al. Can reconstructed Se-deficient line defects in monolayer VSe_2 induce magnetism? *Adv. Mater.* **32**, 2000693 (2020).

11. Avsar, A. et al. Defect induced, layer-modulated magnetism in ultrathin metallic $PtSe_2$. *Nat. Nanotechnol.* **14**, 674–678 (2019).
12. Guguchia, Z. et al. Magnetism in semiconducting molybdenum dichalcogenides. *Sci. Adv.* **4**, eaat3672 (2018).
13. Deng, Y. et al. Gate-tunable room-temperature ferromagnetism in two-dimensional Fe_3GeTe_2. *Nature* **563**, 94–99 (2018).
14. Verzhbitskiy, I. A. et al. Controlling the magnetic anisotropy in $Cr_2Ge_2Te_6$ by electrostatic gating. *Nat. Electron.* **3**, 460–465 (2020).
15. Zhuo, W. et al. Manipulating ferromagnetism in few-layered $Cr_2Ge_2Te_6$. *Adv. Mater.* **33**, 2008586 (2021).
16. Göser, O., Paul, W. & Kahle, H. G. Magnetic properties of CrSBr. *J. Magn. Magn. Mater.* **92**, 129–136 (1990).
17. Beck, J. Über chalkogenidhalogenide des chroms synthese, kristallstruktur und magnetismus von chromsulfidbromid, CrSBr. *ZAAC J. Inorg. Gen. Chem.* **585**, 157–167 (1990).
18. Huang, Y. et al. Reliable exfoliation of large-area high-quality flakes of graphene and other two-dimensional materials. *ACS Nano* **9**, 10612–10620 (2015).
19. Novoselov, K. S. et al. Electric field effect in atomically thin carbon films. *Science* **306**, 666–669 (2016).
20. Telford, E. J. et al. Via method for lithography free contact and preservation of 2D materials. *Nano Lett.* **18**, 1416–1420 (2018).
21. Wang, L. et al. One-dimensional electrical contact to a two-dimensional material. *Science* **342**, 614–617 (2013).
22. Alexander, S., Helman, J. S. & Balberg, I. Critical behavior of the electrical resistivity in magnetic systems. *Phys. Rev. B* **13**, 304–315 (1976).
23. Balberg, I. & Helman, J. S. Critical behavior of the resistivity in magnetic systems. II. Below T_c and in the presence of a magnetic field. *Phys. Rev. B* **18**, 303–318 (1978).
24. Shklovskii, B. I. & Efros, A. L. *Electronic Properties of Doped Semiconductors* 45 (Springer Berlin Heidelberg, 1984).
25. Efros, A. L. & Shklovskii, B. I. Coulomb gap and low temperature conductivity of disordered systems. *J. Phys C* **8**, L49 (1975).
26. Brodowska, B. et al. Magnetoresistance near the ferromagnetic-paramagnetic phase transition in magnetic semiconductors. *Appl. Phys. Lett.* **93**, 42113 (2008).
27. Majumdar, P. & Littlewood, P. B. Dependence of magnetoresistivity on charge-carrier density in metallic ferromagnets and doped magnetic semiconductors. *Nature* **395**, 479–481 (1998).
28. Lin, Z. et al. Pressure-induced spin reorientation transition in layered ferromagnetic insulator $Cr_2Ge_2Te_6$. *Phys. Rev. Mater.* **2**, 051004 (2018).
29. López-Cabrelles, J. et al. Chemical design and magnetic ordering in thin layers of 2D metal–organic frameworks (MOFs). *J. Am. Chem. Soc.* **143**, 18502–18510 (2021).
30. Shukla, A., Lebedev, O. I., Seikh, M. M. & Kundu, A. K. Structural and magnetic characterization of spin canted mixed ferrite-cobaltites: $LnFe_{0.5}Co_{0.5}O_3$ (Ln = Eu and Dy). *J. Magn. Magn. Mater.* **491**, 165558 (2019).
31. Yildiz, F., Przybylski, M. & Kirschner, J. Direct evidence of a nonorthogonal magnetization configuration in single crystalline $Fe_{1-x}Co_x$ / Rh / Fe / Rh(001) system. *Phys. Rev. Lett.* **103**, 147203 (2009).
32. Durst, A. C., Bhatt, R. N. & Wolff, P. A. Bound magnetic polaron interactions in insulating doped diluted magnetic semiconductors. *Phys. Rev. B* **65**, 235205 (2002).
33. Mcguire, T. R. & Potter, R. I. Anisotropic magnetoresistance in ferromagnetic 3D alloys. *IEEE Trans. Magn.* **11**, 1018–1038 (1975).
34. Jansson, F. et al. Large positive magnetoresistance effects in the dilute magnetic semiconductor (Zn,Mn)Se in the regime of electron hopping. *J. Appl. Phys.* **116**, 083710 (2014).
35. Wang, J. et al. Giant magnetoresistance in transition-metal-doped ZnO films. *Appl. Phys. Lett.* **88**, 252110 (2006).
36. Mukherjee, D., Dhakal, T., Srikanth, H., Mukherjee, P. & Witanachchi, S. Evidence for carrier-mediated magnetism in Mn-doped ZnO thin films. *Phys. Rev. B* **81**, 205202 (2010).
37. Coey, J. M. D., Venkatesan, M. & Fitzgerald, C. B. Donor impurity band exchange in dilute ferromagnetic oxides. *Nat. Mater.* **4**, 173–179 (2005).
38. Kittilstved, K. R., Liu, W. K. & Gamelin, D. R. Electronic structure origins of polarity-dependent high-T_c ferromagnetism in oxide-diluted magnetic semiconductors. *Nat. Mater.* **5**, 291–297 (2006).
39. Liu, L. & Liu, J. T. C. Theory of the bound magnetic polaron in antiferromagnetic semiconductors. *Phys. Rev. B* **33**, 1797–1803 (1986).
40. Mauger, A. Magnetic polaron: theory and experiment. *Phys. Rev. B* **27**, 2308–2324 (1983).
41. Shon, W., Rhyee, J. S., Jin, Y. & Kim, S. J. Magnetic polaron and unconventional magnetotransport properties of the single-crystalline compound $EuBiTe_3$. *Phys. Rev. B* **100**, 024433 (2019).
42. Xu, Q. et al. Magnetoresistance and anomalous Hall effect in magnetic ZnO films. *J. Appl. Phys.* **101**, 063918 (2007).
43. Andrearczyk, T. et al. Spin-related magnetoresistance of n-type ZnO:Al and $Zn_{1-x}Mn_xO$:Al thin films. *Phys. Rev. B* **72**, 121309 (2005).
44. Bellingeri, E. et al. Influence of free charge carrier density on the magnetic behavior of (Zn,Co)O thin film studied by field effect modulation of magnetotransport. *Sci. Rep.* **9**, 149 (2019).
45. Xing, G. Z., Yi, J. B., Yan, F., Wu, T. & Li, S. Positive magnetoresistance in ferromagnetic Nd-doped In_2O_3 thin films grown by pulse laser deposition. *Appl. Phys. Lett.* **104**, 202411 (2014).
46. Yang, Z. et al. Electron carrier concentration dependent magnetization and transport properties in ZnO:Co diluted magnetic semiconductor thin films. *J. Appl. Phys.* **104**, 113712 (2008).

Methods

Exfoliation and flake identification. CrSBr flakes were exfoliated onto 285 nm or 90 nm SiO_2/Si^+ substrates using mechanical exfoliation with Scotch Magic tape[47,48]. For devices with greater than one layer of CrSBr, SiO_2/Si^+ substrates were exposed to a gentle oxygen plasma for 5 minutes to remove adsorbates from the surface and increase flake adhesion[18]. The exfoliation was done under ambient conditions by heating the mother tape for 3 minutes at 100 °C, letting it cool to room temperature and then peeling the tape from the substrate as quickly as possible[18]. For devices with monolayer CrSBr, the SiO_2/Si^+ substrates were passivated by depositing a thin layer of 1-dodecanol before exfoliation[9]. The exfoliation was done under inert conditions in a N_2 glove box with <1 ppm O_2 and <1 ppm H_2O content. The mother tape was placed onto the SiO_2/Si^+ substrates without heating and removed as quickly as possible. CrSBr flake thickness was identified using optical contrast before encapsulation and then confirmed with atomic force microscopy after encapsulation with hexagonal boron nitride.

Optical contrast calbration. To more quickly and reliably identify the thickness of CrSBr flakes, a contrast calibration curve was developed for both 285 nm and 90 nm SiO_2/Si^+ substrates. First, a series of images was collected of various CrSBr flakes with varying thicknesses using a Nikon Eclipse LV150N microscope and Nikon DS-Fi3 camera. The images were then shading corrected, in which the inhomogeneous illumination of the substrate across a single image was corrected by dividing by an optical image of a pristine area of the chip without CrSBr flakes. The contrast of the flakes was then extracted using Gwyddion to measure the difference in colour between the substrate and the desired flake. We found that the red colour contrast was the most substantial, so all reported optical contrasts are with respect to red. The series of extracted contrasts was binned into a histogram, and the histrogram was fitted to an N-peak Gaussian, where N is the number of expected flake thicknesses. The extracted positions of the Gaussian peaks provide the average red optical contrast for each CrSBr thickness (Supplementary Figs. 1 and 2). The thicknesses of the flakes were confirmed with atomic force microscopy (Supplementary Fig. 3).

Atomic force microscopy. Atomic force microscopy was performed in a Bruker Dimension Icon using OTESPA-R3 tips in tapping mode. Flake thicknesses were extracted using Gwyddion to measure histograms of the height difference between the substrate and the desired CrSBr flake.

Transport device fabrication. Transport devices were fabricated from CrSBr flakes using the via contact technique[20] in which hexagonal boron nitride with embedded palladium electrodes was placed onto the desired CrSBr flake using the dry-polymer-transfer technique[21]. For CrSBr flakes with greater than one layer, the transfer process was performed under ambient conditions. For monolayer CrSBr flakes, the transfer process was performed under inert conditions in a N_2 glove box with <5 ppm O_2 and <0.5 ppm H_2O. Bonding pads were then designed and deposited using conventional electron beam lithography and deposition techniques. All devices were diced by hand and bonded to a 16-pin dual in-line package socket for measurement in cryogenic systems. Between fabrication steps, one-layer devices were stored in the N_2 glove box to avoid sample degredation.

Electrical transport measurements. Longitudinal resistance was measured in a two-terminal configuration using an SRS830 lock-in amplifier to source voltage and measure current using a 17.777 Hz reference frequency. Four-terminal longitudinal and Hall measurements were performed in a four-terminal configuration using SRS830 lock-in amplifiers to source voltage, measure current and measure the longitudinal/Hall voltage using a 17.777 Hz reference frequency. Due to the morphology of the exfoliated crystals, the current and longitudinal resistances were measured parallel to the a axis, and the Hall resistance was measured parallel to the b axis. Variable temperatures between 1.6 K and 300 K and magnetic fields between −9 T and 9 T were achieved in a Janis pumped ^{4}He cryostat. Sample temperature equilibrium was checked by monitoring sample resistivity for stability over time at a fixed temperature. Hysteresis in the superconducting magnet due to trapped fields was measured by identifying the zero-field shift from the forward and backward field scans measured in the non-magnetic state (at $T = 300$ K). This hysteresis was accounted for in all presented magnetoresistance measurements. For measurements without electrostatic gating, the silicon back gate was kept grounded using a grounding cap. For gate-dependent measurements, a Keithley 2400 was used to output voltages between −60 V and 60 V on the silicon back gate. A protection resistor of 100 kΩ was placed in series between the gate and the voltage source.

The field-direction-dependent transport measurements on monolayer CrSBr were performed using a homemade double-axis rotator in the Janis pumped ^{4}He cryostat. The angle was adjusted at room temperature inside the cryostat to avoid exposing the sample to air between measurement runs. Once the angle was set at room temperature, it was kept fixed for all transport measurements along the chosen crystallographic axis. The angle of the magnetic field relative to the crystallographic axes of CrSBr was determined by orienting the sample relative to the mounted dual in-line package socket by hand and aligning the dual in-line package socket to the probe axis by eye. We estimate an uncertainty in the field angle of ~3°.

Vibrating sample magnetometry. All vibrating sample magnetometry was conducted on a Quantum Design PPMS DynaCool system. A single CrSBr crystal was selected, and the surface was exfoliated mechanically to expose a pristine interface. The crystal was attached to a quartz paddle using GE varnish (which was cured at room temperature under ambient conditions for 30 minutes) and oriented with the a, b or c axis perpendicular to the length of the quartz paddle. The same crystal was used for all axial-orientated measurements. The variable temperature scans and field-dependent magnetic susceptibility curves for each axis were measured during the same measurement cycle. The crystal was removed using a 1:1 ethanol/toluene solution, dried in air and then reoriented and reattached using the previously prescribed varnish method.

Data availability

The data that support the plots within this Article and other findings of this study are available from the corresponding authors upon reasonable request.

References

47. Novoselov, K. S. et al. Electric field in atomically thin carbon films. *Science* **306**, 666–669 (2004).
48. Novoselov, K. S. et al. Two-dimensional atomic crystals. *Proc. Natl Acad. Sci. USA* **102**, 10451–10453 (2005).

Acknowledgements

We thank J. Pack for his help in using the double-axis rotator for the field-direction-dependent transport measurements. We thank T.-D. Li for help performing the X-ray photoelectron spectroscopy measurements. We also thank J. Xiao for helpful discussions in interpreting our transport data. Research on magnetotransport properties of van der Waals magnetic semiconductors was supported as part of Programmable Quantum Materials, an Energy Frontier Research Center funded by the US Department of Energy, Office of Science, Basic Energy Sciences, under award DE-SC0019443. Neutron scattering experiments were performed at the Spallation Neutron Source, a Department of Energy Office of Science User Facility operated by Oak Ridge National Laboratory. A.H.D. was supported by the National Science Foundation graduate research fellowship programme (DGE 16-44869). R.A.W. was supported by the Arnold O. Beckman Fellowship in Chemical Sciences. The Columbia University Shared Materials Characterization Laboratory was used extensively for this research. We are grateful to Columbia University for the support of this facility. The PPMS system used to perform vibrating sample magnetometry and some of the transport measurements was purchased with financial support from the National Science Foundation through a supplement to award DMR-1751949. The electron microscopic work performed at Brookhaven National Laboratory was sponsored by the US Department of Energy, Basic Energy Sciences, Materials Sciences and Engineering Division, under contract no. DE-SC0012704. The X-ray photoelectron microscopy was performed at the Surface Science Core Facility in Advanced Science Research Center of City University of New York.

Author contributions

E.J.T. and A.H.D. prepared the CrSBr flakes. E.J.T. and A.H.D. performed the optical contrast calibration and atomic force microscopy measurements. E.J.T. and R.L.D. fabricated the transport devices and performed the transport measurements. A.H.D. synthesized the bulk crystals. E.J.T. and K.L. performed the Raman spectroscopy measurements. E.J.T., A.H.D. and R.A.W. performed the vibrating sample magnetometry measurements. E.J.T. performed the oxidation measurements. M.-G.H. and Y.Z. performed the transmission electron microscopy imaging. S.S. and A.N.P. performed the scanning tunnelling microscopy measurements. A.H.D. and E.J.T. performed the scanning electron microscopy imaging and energy-dispersive X-ray analysis. All authors contributed to analysing the data and writing the manuscript.

Competing interests

The authors declare no competing interests.

Additional information

Supplementary information The online version contains supplementary material available at https://doi.org/10.1038/s41563-022-01245-x.

Correspondence and requests for materials should be addressed to Cory R. Dean or Xavier Roy.

Peer review information *Nature Materials* thanks Ahmet Avsar and the other, anonymous, reviewer(s) for their contribution to the peer review of this work.